Analysis of ductile damage evolution and failure mechanisms due to reverse loading conditions for the aluminum alloy EN-AW 6082-T6

Zhichao Wei[1,*], **Moritz Zistl**[1], **Steffen Gerke**[1], and **Michael Brünig**[1]

[1] Institut für Mechanik und Statik, Universität der Bundeswehr München, Werner-Heisenberg-Weg 39, 85579 Neubiberg, Germany

This paper deals with experiments and numerical simulations for reverse uniaxial tension-compression and shear tests to investigate the ductile damage and fracture behavior of the aluminum alloy EN-AW 6082-T6. For this purpose, experiments with different loading sequences and number of loading cycles with uniaxial tensile and new shear specimens have been performed. Furthermore, the digital image correlation (DIC) technique captures the deformations and strain fields during the experimental processes. A modified anisotropic stress-state-dependent elastic-plastic-damage continuum model is proposed and is validated by experimental strain fields measured by DIC. Moreover, numerically predicted distributions of the principal damage strains are compared with fracture images taken by scanning electron microscopy (SEM).

1 Introduction

In continuum mechanics the stress triaxiality is widely used to characterize the stress state [1–3]. One of the highlights of the proposed stress-state-dependent anisotropic damage model by Brünig [4] is simulating the effect of different damage mechanisms. For example, the damage is caused by simultaneous growth of voids and formation of micro-shear-cracks and their coalescence under lower positive stress states, see [5]. Thus, studying the damage evolution under different loading conditions (stress states) is interesting. A series of biaxial experiments considering different loading/preloading histories have been performed by Brünig et al. [6] and Zistl et al. [7]. However, a discussion of the effect of reverse loading histories on the onset and evolution of the ductile damage process is still lacking. The present work aims to fill this gap by studying the occurrence and development of damage and fracture behavior under reverse loading conditions.

To capture the Bauschinger effect, a combined hardening law is entered into the proposed elastic-plastic-damage model by Brünig [4]. Uniaxial tensile and shear cyclic tests have been performed to validate the modified constitutive model. This paper is organized as follows. First, the plastic and damage criterion and combined hardening rule are shortly introduced in section 2; for more details, please refer to Wei et al. [8]. Then section 3 describes the identification of the combined hardening parameters and the experimental and numerical results. Finally, conclusions are presented in section 4.

2 Constitutive modeling

The modified phenomenological plastic-damage constitutive model uses the plastic yield condition to characterize the onset of plastic yielding and the plastic flow law to evaluate the inelastic strains caused by plastic deformation. In a similar way, the damage criterion captures the onset of damage and the evolution of the further inelastic strains caused by the formation of micro-defects is governed by the damage rule. For more details, please refer to [4].

As observed in uniaxial tension and compression tests, the compressive yield stress is higher than the tensile stress [8], the so-called strength-differential effect. Therefore, the Drucker-Prager yield criterion with combined isotropic-kinematic hardening is taken into account to analyze the plastic behavior

$$f^{\text{pl}} = \sqrt{\frac{1}{2}\text{dev}(\bar{\mathbf{T}} - \bar{\boldsymbol{\alpha}}) \cdot \text{dev}(\bar{\mathbf{T}} - \bar{\boldsymbol{\alpha}})} + \bar{c}(\frac{a}{\bar{c}}\text{tr}(\bar{\mathbf{T}} - \bar{\boldsymbol{\alpha}}) - 1) = 0\,, \tag{1}$$

where $\bar{\mathbf{T}}$ represents the effective Kirchhoff stress tensor, $\bar{\boldsymbol{\alpha}}$ is the effective back stress tensor, the hydrostatic stress coefficient is measured as $a/\bar{c} = 32\ \text{TPa}^{-1}$ [8], and $\bar{c}$ depicts the equivalent yield stress. Furthermore, an extended Voce hardening law for isotropic hardening

$$\bar{c} = c_0 + Q_1(1 - e^{-p_1\gamma}) + Q_2\xi(1 - e^{-p_2\gamma}) \tag{2}$$

and the modified Chaboche's kinematic hardening model for the rate of the back stress tensor $\dot{\bar{\boldsymbol{\alpha}}}$

$$\dot{\bar{\boldsymbol{\alpha}}} = \dot{\bar{\boldsymbol{\alpha}}}_1 + \dot{\bar{\boldsymbol{\alpha}}}_2 + \dot{\bar{\boldsymbol{\alpha}}}_3 \tag{3}$$

---

* Corresponding author: e-mail zhichao.wei@unibw.de, phone +49 (89) 6004 3413

with

$$\dot{\bar{\boldsymbol{\alpha}}}_1 = b_1\chi\dot{\bar{\mathbf{H}}}^{\mathrm{pl}} - b_2\chi\dot{\gamma}\bar{\boldsymbol{\alpha}}_1$$
$$\dot{\bar{\boldsymbol{\alpha}}}_2 = b_3\dot{\bar{\mathbf{H}}}^{\mathrm{pl}} - b_4\dot{\gamma}\bar{\boldsymbol{\alpha}}_2 \tag{4}$$
$$\dot{\bar{\boldsymbol{\alpha}}}_3 = b_5\dot{\bar{\mathbf{H}}}^{\mathrm{pl}} - (1 - \cos^2\theta)b_6\dot{\gamma}\bar{\boldsymbol{\alpha}}_3\,,$$

are used to model plastic hardening behavior, where Q_1, Q_2 and b_1–b_5 are the hardening moduli, p_1 and p_2 are the hardening exponents, $\dot{\bar{\mathbf{H}}}^{\mathrm{pl}}$ represents plastic strain rate tensor, γ is the equivalent plastic strain, and the function variables ξ and χ are used to capture hardening at the beginning of the plastic deformation phase more accurately, as defined in [8]. θ describes the angle between the third effective back stress term $\bar{\boldsymbol{\alpha}}_3$ and effective reduced stress tensor $(\bar{\mathbf{T}} - \bar{\boldsymbol{\alpha}})$

$$\cos^2\theta = \frac{((\bar{\mathbf{T}} - \bar{\boldsymbol{\alpha}}) \cdot \bar{\boldsymbol{\alpha}}_3)^2}{\left\|\bar{\mathbf{T}} - \bar{\boldsymbol{\alpha}}\right\| \left\|\bar{\boldsymbol{\alpha}}_3\right\|}\,, \tag{5}$$

which is used to activate or deactivate the recovery term in the third component of the back stress rate tensor. As the numerical results show that the angle θ is nearly equal to 0 in the case of the uniaxial tensile test, whereas the angel θ changes obviously during the loading process for the shear test [8]. In addition, the total hardening rate $\dot{\sigma}$ is an additive combination of equivalent stress rate $\dot{c}$ and back stress rate $\dot{\alpha}$

$$\dot{\sigma} = \rho\dot{c} + (1 - \rho)\dot{\alpha}\,, \tag{6}$$

where hardening ratio ρ describes the proportion of isotropic hardening identified by simple uniaxial cyclic loading inversely.

Furthermore, the damage criterion f^{da} expressed in terms of the first stress invariant I_1 and the second deviatoric stress invariant J_2

$$f^{\mathrm{da}} = \alpha I_1 + \beta\sqrt{J_2} - \tilde{\sigma} = 0 \tag{7}$$

as well as the damage strain rate containing an isotropic volumetric part corresponding to the growth of voids and a deviatoric part corresponding to formation of micro-shear-cracks is defined

$$\dot{\mathbf{H}}^{\mathrm{da}} = \dot{\mu}(\tilde{\alpha}\frac{1}{\sqrt{3}}\mathbf{1} + \tilde{\beta}\tilde{\mathbf{N}})\,, \tag{8}$$

where α, β, $\tilde{\alpha}$, and $\tilde{\beta}$ are stress-state-dependent variables based on the stress triaxiality η and the Lode parameter ω, $\dot{\mu}$ represents the equivalent damage strain rate, and $\tilde{\mathbf{N}}$ is the transformed normalized deviatoric stress direction. The stress triaxiality η is defined as the ratio of hydrostatic stress and the von Mises equivalent stress σ_{eq}

$$\eta = \frac{\sigma_{\mathrm{m}}}{\sigma_{\mathrm{eq}}} = \frac{I_1}{3\sqrt{3J_2}}\,, \tag{9}$$

and the Lode parameter

$$\omega = \frac{2T_2 - T_1 - T_3}{T_1 - T_3} \quad \text{with} \quad T_1 \geq T_2 \geq T_3 \tag{10}$$

describes the deviatoric stress state, which is calculated in terms of the principal stresses T_i.

3 Parameter identification

Isotropic and kinematic hardening parameters are determined using the least square method based on the monotonic tensile test. The experimentally obtained original force-displacement curve is converted into the equivalent stress c - equivalent plastic strain γ curve (Fig. 1 (a)), and back stress α- equivalent plastic strain γ curve (Fig. 1 (b)), respectively, for parameter fitting. The fitted curves show good agreement with the experimental results, as shown in Fig. 1, and the correlative isotropic/kinematic hardening parameters are shown in the Tab. 1. It is worth mentioning that the yield point in the present work is defined as the Cauchy stress corresponding to 0.01% plastic strain since the identification of yield stress affects the hardening behavior, as pointed out by Abdel-Karim [9]. Thus, the yield stress is around 240.7 MPa which is lower than the standard yield stress, with a value of 285 MPa corresponding to 0.2% plastic strain. As described in Eq. (2), c_0 is the initial equivalent stress, which is $1/\sqrt{3}$ of the yield stress, i.e., $c_0 = 139$ MPa. Regarding the Chaboche kinematic hardening components, α_1 describes the plastic deformation at the beginning of the yielding, after which it remains nearly constant outside this transition stage. As a result, the exponential parameter b_2 should be large enough to rapidly diminish the first back stress term

α_1. Additionally, as shown in Eq.(4), α_3 includes an active/deactivate recovery term, which has nearly no influence on the monotonic tensile test [8]. Hence, α_3 is assumed to be a linear term, and the value of hardening moduli b_5 is approximately equal to the stress-strain slope at the end of the loading phase. In addition, b_6 can be inversely identified by the monotonic tensile shear loading, the numerical results taking into account three different coefficients b_6 are shown in Fig. 2. As observed in Fig. 2(a), there is no significant difference between force-displacement responses before point A ($\Delta u_{\text{ref}} = 0.6$ mm) when b_6 parameters are varied since the angle parameter $\cos^2 \theta$ is almost close to 1 [8]. However, with an increases in b_6, the slope between the two points of the force-displacement curve AB decreases. As shown in Fig. 2(a), the numerical result is overestimated with $b_6 = 0$ compared to the experimental result, whereas the numerical result with $b_6 = 13.5$ is underestimated. Furthermore, the numerical results for the tensile test in Fig. 2(b) indicate that the mentioned kinematic hardening parameter b_6 has almost no effect on the force-displacement response undergoing tensile test.
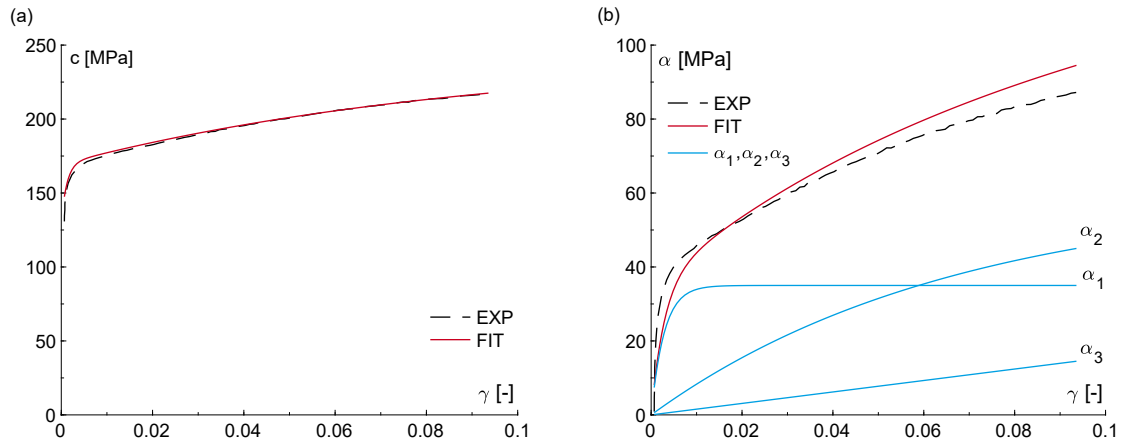

Fig. 1: Parameter identification: (a) equivalent stress c vs. equivalent plastic strain γ curve fitting for the isotropic hardening, (b) back stress α vs. equivalent plastic strain γ curve fitting for kinematic hardening, and three back stress components are plotted in the solid blue lines, respectively.
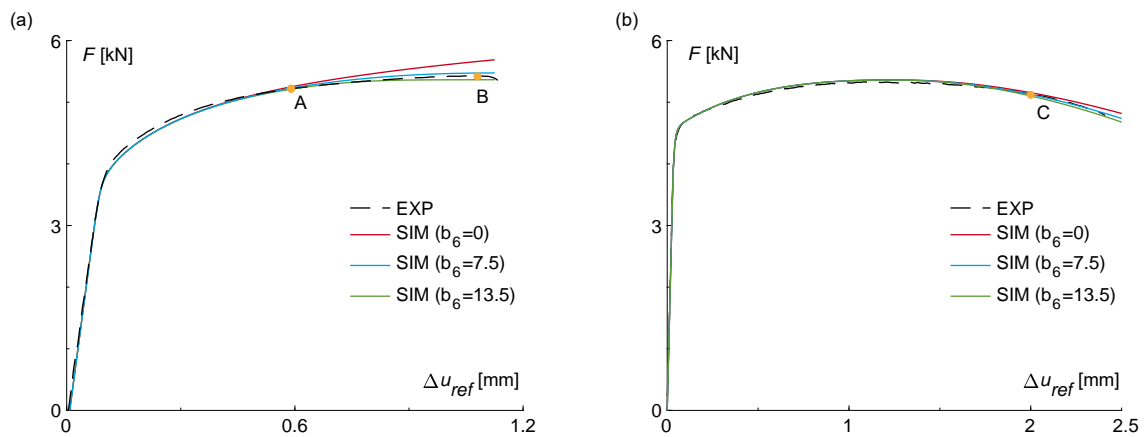

Fig. 2: The force-displacement responses of the shear test (a) and uniaxial tensile test (b) taking into account different kinematic hardening parameters b_6 (see Eq. (4)).

Table 1: Material parameters.

c_0[MPa]	Q_1[MPa]	Q_2[MPa]	p_1[−]	p_2[−]	ρ[−]
139	74.93	21.31	8.96	676.01	0.41
b_1[MPa]	b_2[−]	b_3[MPa]	b_4[−]	b_5[MPa]	b_6[−]
12250	350	895	15	155	7.5

The hardening ratio ρ plays an essential role in capturing the Bauschinger effect. The change of hardening ratio ρ results in a change in the numerical yield stress under reverse loading. It seems that the hardening ratio ρ could be a function or a constant value. To simplify the material model, the hardening ratio ρ is assumed to be constant. To avoid the damage and
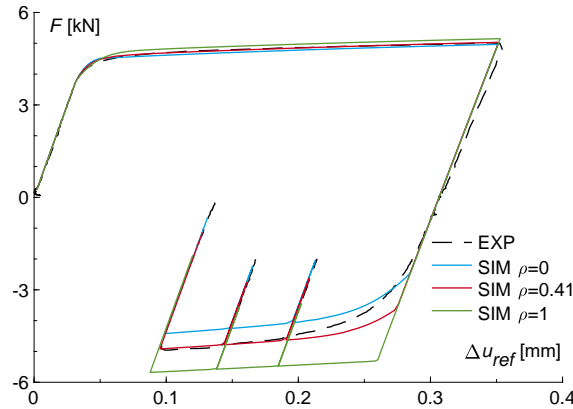
Fig. 3: Experimental and numerical force F vs. displacement Δu_{ref} curves for uniaxial tension-compression (TC) with unloading after compression: experimental data are plotted in black dashed line, solid blue line represents simulation with the pure kinematic hardening ($\rho = 0$), solid green line is the simulation with pure isotropic hardening ($\rho = 1$), and solid red line depicts the simulation with combined hardening ($\rho = 0.41$).

buckling affecting the yield stress after reverse loading, the uniaxial tension-compression (TC) test loaded in a small strain range is used to calibrate the hardening ratio ρ inversely. As shown in Fig. 3, the predicted yield stress under compression using isotropic hardening ($\rho = 1$) is significantly greater than one taking into account only kinematic hardening $\rho = 0$. It is clearly demonstrated that the pure isotropic/kinematic hardening leads to over- or underestimation of the yield stress after reverse loading. However, a combined hardening with the hardening ratio $\rho = 0.41$ shows very good agreement with the experimental result. Furthermore, the pure Voce isotropic hardening cannot capture the nonlinear properties after reverse loading. The Chaboche kinematic and combined hardening model involving three back stress components can, however, describe the nonlinearity after reverse loading, as shown in Fig. 3.

In addition, the stress-state-dependent variables α, β, $\tilde{\alpha}$, and $\tilde{\beta}$ in the damage model are identified by examining the behavior of a unit cell containing micro-void with 3% initial void volume fraction. The aim of this work is to find the mentioned stress-state-dependent parameters suitable for a wide class of the ductile metals, and the micro-numerical analysis and corresponding material parameters have been presented by Brünig et al. [10]. Most important, those parameters have been validated by doing series of experiments and numerical simulations with different metals: for aluminum alloy EN-AW 6082 [7,8] and ductile steel X5CrNi18-10 [11].

4 Experimental and numerical results

In experiments, different cyclic loading patterns have been performed to study the influence of loading sequence and reverse loading on the onset and evolution of damage and fracture behavior. As mentioned in the introduction, the damage mechanisms are different under different stress states. For example, the damage is caused by the growth of micro-voids in tensile tests, whereas the damage occurs due to the formation and coalescence of the micro-shear-cracks for shear tests. Thus, various uniaxial tensile tests and shear tests have been performed in the current work.

The experimental and numerical force-displacement curves and the photo of tension-compression and shear specimen are shown in Fig. 4, respectively. Moreover, the comparison between experimental and numerical predicted force F and the maximum value of first principal strain A_1 on the surfaces of the specimens just before the failure are listed in Tab. 2. The numerical results show good agreement with experiments for the global force-displacement responses (Figs. 4(a)-(d)) and the local strain level, as shown in Tab. 2 for different loading patterns. In addition, the specimens undergoing cyclic loading failed earlier than after corresponding monotonic loading. The scanning electron microscopy (SEM) clearly shows that more coarse dimples and voids can be observed under reverse loading conditions compared to the monotonic loading [8]. This trend can also be observed in shear tests. It indicates that the more intense and accessible coalescence of micro-defects caused by reverse loading leads to more brittle material behavior.

Furthermore, Fig. 4(g) depicts the distribution of the stress triaxiality η and Lode parameter ω in the notched cross-section of the shear specimen. The average value of the stress triaxiality and the Lode parameter over the notched cross-section area is defined as, respectively

$$\bar{\eta} = \frac{1}{S} \int_0^S \eta \, ds \quad \text{and} \quad \bar{\omega} = \frac{1}{S} \int_0^S \omega \, ds, \tag{11}$$

where S is the total area of the corresponding cross-section. Also, Fig. 5 shows the average value of the stress triaxiality $\bar{\eta}$ and $\bar{\omega}$ which changes only slightly during the investigated loading processes. For example, the average stress triaxiality $\bar{\eta}$ is

PAMM · Proc. Appl. Math. Mech. **22**:1 (2022)

5 of 6

Table 2: Comparison between experimental and numerical results for the force F and the first principal strain A_1 on the surfaces of the specimens just before failure.

Loading patterns		EXP		SIM		Error (%)	
		F [kN]	A_1 [-]	F [kN]	A_1 [-]	F [kN]	A_1 [-]
Uniaxial tensile tests	mon-T	5.00	0.34	4.98	0.36	-0.40	5.88
	cyc-TCT	4.92	0.28	5.01	0.28	1.83	0.00
	cyc-TCTCT	5.09	0.33	5.14	0.35	0.98	6.06
Shear tests	mon-T	5.42	0.57	5.51	0.62	1.7	8.77
	cyc-TCT	5.39	0.39	5.40	0.43	0.19	10.26
	cyc-TCTCT	5.23	0.43	5.40	0.45	3.25	4.65

around $0.1 - 0.2$, and the average Lode parameter $\bar{\omega}$ varies from -0.2 to -0.15. Therefore, the current shear specimen is suitable for studying the damage behavior in positive and negative (reverse loading) lower stress triaxiality regions.
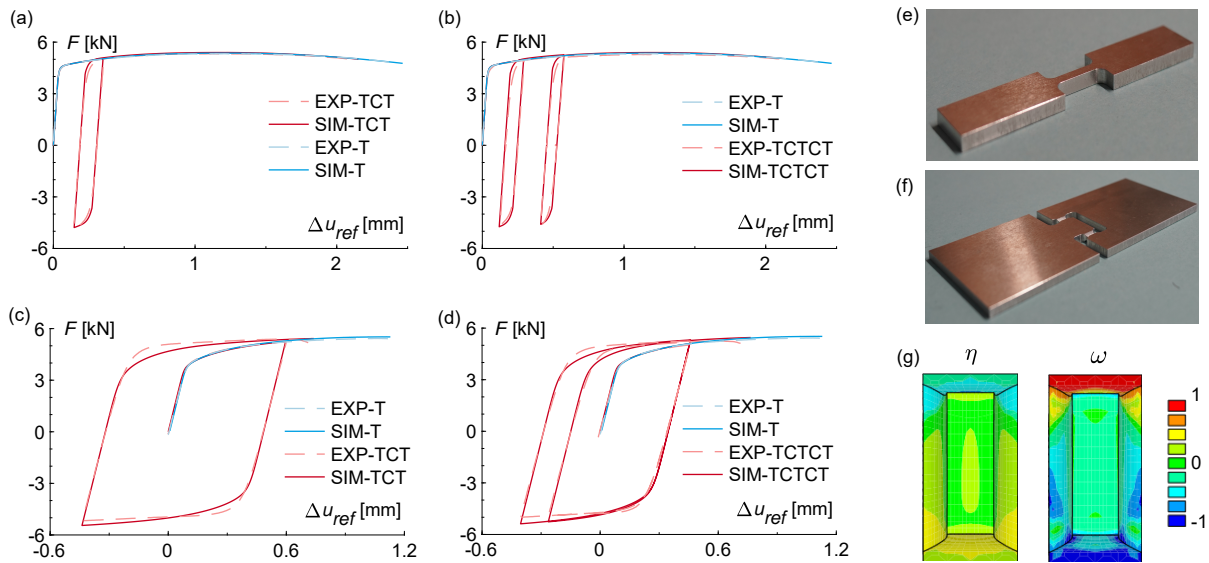

Fig. 4: Force F vs. displacement Δu_{ref} for uniaxial tension-compression ((a) and (b)) and shear tests ((c) and (d)), the photo of TC-specimen (e) and shear specimen (f), and the distribution of stress triaxiality η and Lode parameter ω in the notched cross-section for the shear specimen under monotonic loading (g)
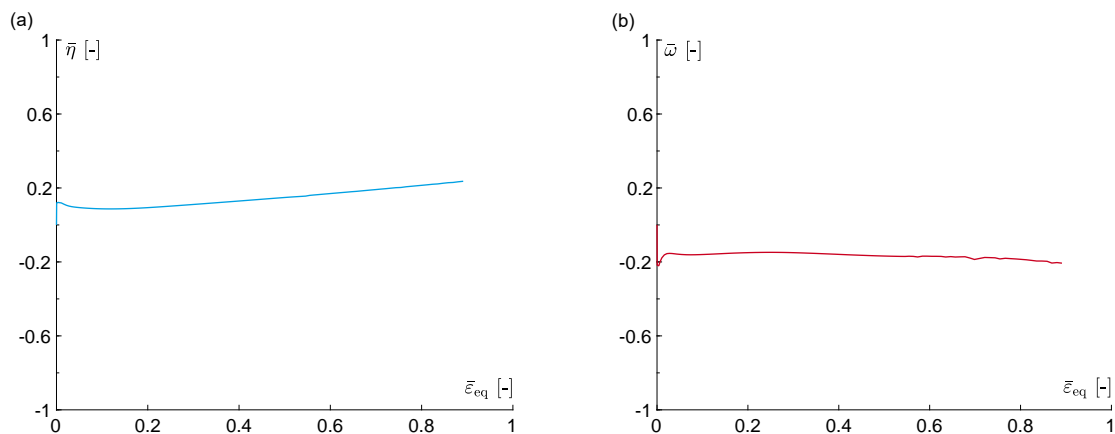

Fig. 5: The average value of the stress triaxiality $\bar{\eta}$ and $\bar{\omega}$ versus the average value of the equivalent strain $\bar{\varepsilon}_{\text{eq}}$ over the notched cross-section of the shear specimen.

The average value of the stress triaxiality $\bar{\eta}$ and $\bar{\omega}$ in the TC-specimen and shear specimen cross-section, and the predicted maximum principal damage stress A_1^{da} just before failure are represented in Tab. 3. Additionally, the damage strain invariants $(I_1^{\text{da}}, I_2^{\text{da}}, \text{and } I_3^{\text{da}})$ for the critical point (where has the maximum principal damage strain), as shown in Tab. 3. Also, the average value of the stress triaxiality $\bar{\eta}$ and $\bar{\omega}$ for monotonic loading and cyclic loading show no apparent difference, see

Table 3: Comparison stress-state parameters ($\bar{\eta}$ and $\bar{\omega}$) and damage strain invariants in the critical positions just before failure between uniaxial tensile and shear tests.

Loading patterns		stress-state parameters		damage strain invariants in critical positions				
		$\bar{\eta}$	$\bar{\omega}$	A_1^{da}	I_1^{da}	$\sqrt{I_2^{\mathrm{da}}}$	$\sqrt[3]{I_3^{\mathrm{da}}}$	surface or cross-section
Uniaxial tensile tests	mon-T	0.42	-0.9	0.0105	0.00666	0.00839	0.00129	cross-section
	cyc-TCT	0.39	-0.9	0.0030	0.00123	0.00169	0.00041	cross-section
	cyc-TCTCT	0.41	-0.9	0.0084	0.00406	0.00514	0.00085	cross-section
Shear tests	mon-T	0.19	-0.18	0.0063	0.00074	0.01035	-0.00242	notch's surface
	cyc-TCT	0.14	-0.13	0.0090	0.00065	0.01085	0.00443	notch's surface
	cyc-TCTCT	0.15	-0.15	0.0209	0.00160	0.02583	0.01108	notch's surface

Tab. 3. In addition, the maximum value of the first damage strain A_1^{da} is observed in the center of the cross-section of the TC-specimen, whereas it occurs in the notched surface of the shear specimen. Moreover, it can be observed that the first damage strain invariant I_1^{da} for uniaxial tension tests is significantly greater than for shear tests since the micro-voids grow predominantly in the direction of tension rather than shear. On the contrary, the roots of the second damage strain invariant $\sqrt{I_2^{\mathrm{da}}}$ and the third damage strain invariant $\sqrt[3]{I_3^{\mathrm{da}}}$ have a sizeable significant influence compared to the first damage strain invariant I_1^{da} undergoing shear loading. This observation suggests that the fracture criterion based on the state of damage strain proposed by Brünig et al. [12] is reasonable.

5   Conclusions

A modified anisotropic stress-state-dependent elastic-plastic-damage model is used to predict damage onset and evolution under reverse loading conditions. The tensile and shear monotonic, cyclic experiments are used to validate the proposed continuum model, and the numerical results are in good agreement with the experiments. As observed in experiments, the reverse loading builds more coarse dimples, making the material more brittle. It can be seen that the number of loading cycles and sequences affects the damage behavior and its evolution.

References

[1] Z. Peng, H. Zhao, and X. Li, New ductile fracture model for fracture prediction ranging from negative to high stress triaxiality, International Journal of Plasticity **145**, 103057 (2021).

[2] F. Yu, P.-Y. Ben Jar, and M. Hendry, Constitutive analysis of pressure-insensitive metals under axisymmetric tensile loading: A stress triaxiality-dependent plasticity damage mode, International Journal of Mechanical Sciences **142**, 21-32 (2018).

[3] X. Gao, G. Zhang, and C. Roe, A study on the effect of the stress state on ductile fracture, International Journal of Damage Mechanics **19(1)**, 75-94 (2010).

[4] M. Brünig, An anisotropic ductile damage model based on irreversible thermodynamics, International Journal of Plasticity **19**, 1679–1713 (2003).

[5] M. Brünig, O. Chyra, D. Albrecht, L. Driemeier and M. Alves, A ductile damage criterion at various stress triaxialities, International Journal of Plasticity **24(10)**, 1731–1755 (2008).

[6] M. Brünig, M. Zistl and S. Gerke, Numerical analysis of experiments on damage and fracture behavior of differently preloaded aluminum alloy specimens, Metals **11(3)**, 381 (2021).

[7] M. Zistl, M. Brünig, and S. Gerke, Analysis of damage and fracture behavior in ductile metal sheets undergoing compression and shear preloading, International Journal of Material Forming **15(4)**, 1–14 (2022).

[8] Z. Wei, M. Zistl, S. Gerke, and M. Brünig, Analysis of ductile damage and fracture under reverse loading, International Journal of Mechanical Sciences **228**, 107476 (2022).

[9] M. Abdel-Karim, Effect of elastic modulus variation during plastic deformation on uniaxial and multiaxial ratchetting simulations, European Journal of Mechanics-A/Solids **30(1)**, 11-21 (2011).

[10] M. Brünig, S. Gerke, and V. Hagenbrock, Micro-mechanical studies on the effect of the stress triaxiality and the Lode parameter on ductile damage, International Journal of Plasticity **50**, 49-65 (2013).

[11] M. Brünig, M. Schmidt, and S. Gerke, Numerical analysis of stress-state-dependent damage and failure behavior of ductile steel based on biaxial experiments, Computational Mechanics **68**, 1-11 (2021).

[12] M. Brünig, S. Gerke, and V. Hagenbrock, Stress-state-dependence of damage strain rate tensors caused by growth and coalescence of micro-defect, International Journal of Plasticity **63**, 49–63 (2014).